

Grain boundary effect on structural, optical, and electrical properties of sol–gel synthesized Fe-doped SnO2 nanoparticles

Archana V1, Lakshmi Mohan1,2,†, Kathirvel P3, and Saravanakumar S4

Citation: Chin. Phys. B, 2021, 30 (**4**): 048202. DOI: 10.1088/1674-1056/abc2c1
Journal homepage: http://cpb.iphy.ac.cn; http://iopscience.iop.org/cpb

What follows is a list of articles you may be interested in

Effect of grain boundary energy anisotropy on grain growth in ZK60 alloy using a 3D phase-field modeling

Yu-Hao Song(宋宇豪), Ming-Tao Wang(王明涛), Jia Ni(倪佳), Jian-Feng Jin(金剑锋), and Ya-Ping Zong(宗亚平)
Chin. Phys. B, 2020, 29 (**12**): 128201. DOI: 10.1088/1674-1056/abad1f

Lorentz transmission electron microscopy for magnetic skyrmions imaging

Jin Tang(汤进), Lingyao Kong(孔令尧), Weiwei Wang(王伟伟), Haifeng Du(杜海峰), Mingliang Tian(田明亮)
Chin. Phys. B, 2019, 28 (**8**): 087503. DOI: 10.1088/1674-1056/28/8/087503

Enhanced ionic conductivity in LAGP/LATP composite electrolyte

Shi-Gang Ling(凌仕刚), Jia-Yue Peng(彭佳悦), Qi Yang(杨琪), Ji-Liang Qiu(邱纪亮), Jia-Ze Lu(卢嘉泽), Hong Li(李泓)
Chin. Phys. B, 2018, 27 (**3**): 038201. DOI: 10.1088/1674-1056/27/3/038201

Interfacial transport in lithium-ion conductors

Shaofei Wang(王少飞) and Liquan Chen(陈立泉)
Chin. Phys. B, 2016, 25 (**1**): 018202. DOI: 10.1088/1674-1056/25/1/018202

Grain boundary effect on structural, optical, and electrical properties of sol–gel synthesized Fe-doped SnO_2 nanoparticles

Archana V[1], Lakshmi Mohan[1,2,†], Kathirvel P[3], and Saravanakumar S[4]

[1] *Department of Sciences, Amrita School of Engineering, Coimbatore, Amrita Vishwa Vidyapeetham, India*

[2] *Research and Development Center, Bharathiar University, Coimbatore-641046, Tamilnadu, India*

[3] *GRD Center for Materials Research, Department of Physics, P S G College of Technology, Coimbatore-641004, Tamilnadu, India*

[4] *Department of Physics, N S S College, Pandalam-689501, Kerala, India*

(Received 11 July 2020; revised manuscript received 27 September 2020; published online 20 December 2020)

Tin oxide (SnO_2) and iron-doped tin oxide ($Sn_{1-x}Fe_xO_2$, $x = 0.05$ wt%, 0.10 wt%) nanoparticles are synthesized by the simple sol–gel method. The structural characterization using x-ray diffraction (XRD) confirms tetragonal rutile phases of the nanoparticles. The variations in lattice parameters and relative intensity with Fe-doping concentration validate the incorporation of iron into the lattice. The compressive strain present in the lattice estimated by using peak profile analysis through using Williamson–Hall plot also exhibits the influence of grain boundary formation in the lattice. The radiative recombination and quenching observed in optical characterization by using photoluminescence spectrum (PL) and the shift in the band gap estimated from UV-visible diffused reflectance spectrum corroborate the grain boundary influence. Raman spectrum and the morphological analysis by using a field emission scanning electron microscope (FESEM) also indicate the formation of grain boundaries. The compositional analysis by using energy dispersive x-ray spectrum (EDAX) confirms Fe in the SnO_2 lattice. The conductivity studies exhibit that the impendence increases with doping concentration increasing and the loss factor decreases at high frequencies with doping concentration increasing, which makes the $Sn_{1-x}Fe_xO_2$ a potential candidate for device applications.

Keywords: sol–gel, compressive strain, grain boundary, AC conductivity

PACS: 82.33.Ln, 75.75.Fk, 72.80.Ey, 74.62.Dh **DOI:** 10.1088/1674-1056/abc2c1

1. Introduction

Metal–oxide nanostructures are a part of advances in material science due to their remarkable optoelectronic, thermal, catalytic, photochemical, electrical, and mechanical properties.[1] Among the metal oxides, tin oxide holds a place as an important material. The tin oxide exists in two oxidation states, *i.e.*, +4 as stannic oxide (SnO_2) and +2 as stannous oxide (SnO) respectively. The SnO_2 is the stable form which can be synthesized through low-temperature easier routes. It is an n-type semiconductor having a wide band gap (3.6 eV).[2] It is one of the most promising metal oxides and found to have variety of applications in sensing, liquid crystal displays, solar cells as transparent conducting electrodes, lithium ion batteries, photo catalysis, *etc*.[3–8] The SnO_2 nanostructure has also got relevance as the electrical and structural properties of SnO_2 and can be tuned to enhance the properties. SnO_2 can exist in three crystalline phases: tetragonal rutile phase, cubic phase, and orthorhombic phase, of which, the tetragonal rutile phase is the most stable crystalline phase and can be quite synthesized under normal laboratory conditions. The tetragonal rutile structure of SnO_2 has tin and oxygen atoms with 6 and 4 co-ordinations, respectively. Various synthesis methods have been adopted through aqueous routes, such as hydrothermal,[9,10] solvothermal,[11,12] green synthesis,[13] chemical precipitation,[14,15] and sol–gel methods.[16–18] Among these methods the sol–gel technique was adopted in the present study, for it provides an easy way to obtain better homogeneity, controlled stoichiometry, and high purity.[16] The properties of metal oxides can be tailored through various techniques such as controlling morphology, calcination, surface modification, doping, *etc*.[19,20] Considerable enhancement in the structural, electrical, and electronic properties of SnO_2 has already been reported by being doped with appropriate materials.[21] Doping with transition metal is found to have a deep influence on the properties of the tin oxide.[22–28] One of the most commonly observed consequence of doping is the segregation of dopants or impurities at the grain boundaries.[29] This results in the segregation of defects at the grain boundaries which in turn can affect material properties.[30,31]

The goal of the present research reported in this paper is to investigate the structural, optical, morphological, compositional, vibrational, and conductivity characteristics of the undoped SnO_2 and Fe-doped SnO_2 nanoparticles synthesized by using a simple sol–gel synthesis method. The grain boundary influence on the properties of the doped SnO_2 is discussed in detail.

†Corresponding author. E-mail: lakshmi_mohan@cb.amrita.edu

© 2021 Chinese Physical Society and IOP Publishing Ltd

2. Materials and methods

2.1. Experimental procedure

Stannous chloride dihydrate ($SnCl_2.2H_2O$), ferric nitrate nonahydrate ($Fe(NO_3)_3.9H_2O$), and 25% aqueous ammonia are chemicals for synthesis with polyvinylpyrrolidone ($(C_6H_9NO)_n$) as surfactant were of AR grade and was directly used without any purification. The iron-doped tin-oxide nanoparticles were synthesized by the sol–gel method. A transparent solution was prepared by mixing a 0.2-M aqueous solution of stannous chloride dihydrate ($SnCl_2 \cdot 2H_2O$) which was first dissolved in HCl and 5 ml of ethanol under constant stirring. After the stannous chloride was completely dissolved, a small amount of ferric nitrate nonahydrate ($Fe(NO_3)_3.9H_2O$) was added followed with the addition of 0.2-g PVP into in 4-ml aqueous solution. Aqueous ammonia solution was added dropwise in order to maintain a pH of 8 and continued stirring for 1 h. After that, the solution was allowed to settle overnight. The resulting gel was filtered, washed with water and ethanol to remove impurities, and dried at 100 °C for 12 h. Finally, the sample was crushed and annealed at 600 °C for 4 h forming the iron-doped tin oxide nano powders. The same procedure was repeated but by changing the concentration of the ferric nitrate by 5 wt% and 10 wt%, separately. The chemical reaction equation is as follows:

$$SnCl_4 + 4NH_4OH \longrightarrow Sn(OH)_4 + 4NH_4Cl. \quad (1)$$

Tin hydroxide is calcined to obtain the tin oxide as follows:

$$Sn(OH)_4 \longrightarrow SnO_2 + 2H_2O. \quad (2)$$

2.2. Material characterization

Several characterization techniques were employed to analyze the structural, optical, morphological, and electrical properties of undoped SnO_2 and 5-wt%, 10-wt% Fe-doped SnO_2. The x-ray diffractogram analysis was performed by XRD Philip PW1700 with source Cu $K\alpha$ radiation of wavelength 1.54 Å. The UV-diffused reflectance spectra recorded in a wavelength range of 200 nm–900 nm by JASCO UV-Vis spectrometer (model name: –V-700) were used to study the optical reflectance and absorbance of the undoped and doped SnO_2. The room-temperature analyses of photoluminescence (PL) of all samples were recorded by using a JASCO FLUROSCENCE spectroscope (model name: –FP-8300) with a xenon (Xe) lamp at an excitation wavelength of 300 nm. Raman spectrum was recorded by using Bruker RFS 27 with a laser source Nd:YAG (1064 nm). The field emission scanning electron microscope (FESEM) imaging and energy dispersive analysis of x-ray (EDAX) spectra were conducted by using the CARL ZEISS microscope (model name: ZEISS, SIGMA). The conductivity studies was carried out by using Keithely electrometer 6517B/E and Hioki 3532-50 LCR Meter in a frequency range from 50 Hz to 5 MHz.

3. Results and discussion

3.1. Structural analysis

The x-ray diffractogram of SnO_2 and $Sn_{1-x}Fe_xO_2$ ($x =$ 0.05 wt%, 0.10 wt%) samples were recorded in θ–2θ geometry from a scan range from 20° to 70°. The x-ray diffraction patterns of SnO_2 (shown in Fig. 1) are used to identify the crystalline structure and related lattice parameters. Comparing with the standard JCPDS data (71-0652) lattice planes (110), (101), (200), (111), (211), (220), (002), (310), (112), (301), (202), (321) oriented in the direction of observed peaks are indexed and the peaks correspond to rutile tetragonal structure of tin oxide nanoparticles.

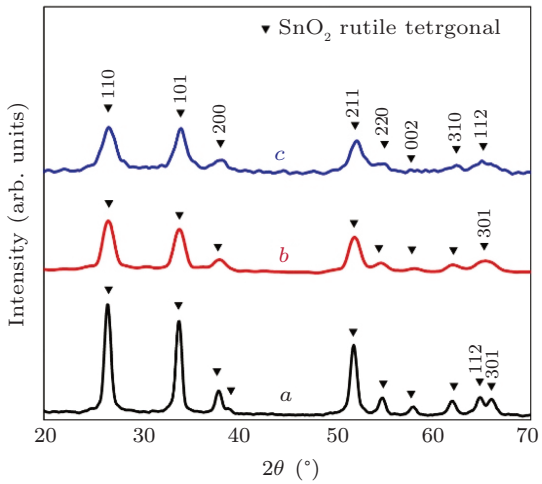


Fig. 1. The XRD pattern of undoped SnO_2 (curve *a*), $Sn_{0.95}Fe_{0.05}O_2$ (curve *b*), and $Sn_{0.90}Fe_{0.10}O_2$ (curve *c*) nanoparticles.

The sharp and intense diffraction peaks indicate the polycrystal line natures of the samples. No traces of impurities are observed, which is attributed to the formation of the pure phase. The average crystalline size is estimated from the Scherrer's formula[32] (Eq. (1)) and tabulated in Table 1.

$$D = \frac{k\lambda}{\beta \cos\theta}, \quad (3)$$

in the above equation, λ is the wavelength of Cu-$K\alpha$ radiation (1.54 Å), θ is the Bragg angle of the corresponding peaks, β is the full width half maximum (FWHM) value, and k is the shape factor.

A decrease in crystalline size is observed with Fe doping and the shift in FWHM is also observed indicating the incorporation of Fe into the SnO_2 lattice. The lattice parameters based on the first approximation are also calculated for tetragonal rutile structure and tabulated in Table 1.[33] The lattice constant ratio obtained is also in good agreement with the standard data (JCPDS: –71-0652). The shrinkage of lattice parameter can be attributed to the substitution of Fe^{3+} ions (0.63 Å) for Sn^{4+} (0.69 Å) site.[33] As reported by Sabri *et al.*[34] the solubility

Table 1. Lattice parameters of SnO_2 and Fe-doped SnO_2 nanoparticles.

Samples	2θ (°)	FWHM (°)	Plane (hkl)	D (nm)	c/a ratio (10^{-3})	Volume (10^{-3} nm^3)	Interplanar spacing (10^{-3} nm)	Shorter bond length (10^{-3} nm)	Longer bond length (10^{-3} nm)
SnO_2	26.522	0.715	110	11.926	0.67 ± 2.9	0.07 ± 2.7	0.33 ± 1.9	0.16 ± 1.3	0.24 ± 0.4
$Sn_{0.95}Fe_{0.05}O_2$	26.578	0.812	110	10.496	0.67 ± 2.3	0.07 ± 2.8	0.33 ± 0.1	0.16 ± 0.3	0.24 ± 1.9
$Sn_{0.90}Fe_{0.10}O_2$	26.646	1.707	110	4.992	0.67 ± 1.1	0.07 ± 7.1	0.33 ± 19.1	0.16 ± 2.5	0.24 ± 1.8

limit of Fe in SnO_2 increases up to 5 wt% in Fe-dopant concentration and above this limit, the diffusion rate lowers and dopants get segregated to the boundaries, which is attributed to the decrease in crystalline size.[35] Reduction in relative intensity with doping (Fig. 1) along with the reduction in grain size confirms that Fe doping hinders the crystallization.[36] The segregation of Fe near the boundary results in the decrease of grain boundary energy, which is favorable for the aggregation on nanoparticles at the grain boundaries.[37]

These grain boundaries as well as the difference between ionic radii of Fe^{3+} ion and Sn^{4+} ion can also induce a strain in the lattice,[38,39] which can induce the XRD peaks to broaden. The micro strain in the lattice and other microstructural evaluations are analyzed by using various models based on Williamson hall plots.

3.2. Peak profile analysis

The x-ray peak broadening arises due to the deviation from ideal crystalline lattice which is infinitely large and has a perfectly ordered crystalline array. Different atoms in the unit cell have divergent scattering power, hence the diffracted wave undergoes the phase shift and changes its amplitude. All imperfections of the sample and instrumental errors contribute to the noticeable broadening of the observed peak profiles. Broadening due to sample related contribution arises from the sample imperfections, crystalline size, micro strain and other defects.

$$\beta_{hkl}^2 = \left(\beta_{hkl}^2\right)_{\text{measured}} - \left(\beta_{hkl}^2\right)_{\text{instrumental}}. \tag{4}$$

The net broadening due to size broadening (β_D) and strain broadening (β_s) given by Eq. (4) is known as the Williamson–Hall equation[40,41]

$$\beta_{hkl} = \frac{k\lambda}{D\cos\theta} + 4\varepsilon\tan\theta. \tag{5}$$

The models employed to collate and confirm the incorporation of Fe into the synthesized sample are as follows: (i) uniform deformation model (UDM), (ii) uniform stress deformation model (USDM), and (iii) uniform deformation energy density model (UDEDM)[42] (Figs. 2–4). The slope values obtained from these methods are tabulated in Table 2. It can be seen that the values obtained for the slopes are negative indicating that the compressive strain in lattice might be due to the shrinkage of lattice compared with its standard values. As crystalline size decreases, higher lattice strain can be expected which leads the XRD peaks to broaden. Thus, the lattice parameter shrinkage and defects lead to compressive strain. The values of the six independent elastic compliance values for rutile tetragonal SnO_2 are calculated by the substitution of elastic stiffness constants (C_{ij} (in unit GPa)).[32,43] As observed from the figures, all the samples (SnO_2, $Sn_{0.95}$ $Fe_{0.05}O_2$, and $Sn_{0.90}Fe_{0.10}O_2$) exhibit negative slopes, thus implying the compressive strain in lattice. The lattice expansion and shrinkage along with crystal defects are the responsible for this strain. The geometrical parameters of SnO_2 and (5 wt%, 10 wt%) Fe-doped tin oxide are listed in Table 2. It can also be concluded from the micro strain that the presence of grain boundaries in the lattice leads to the compressive strain.

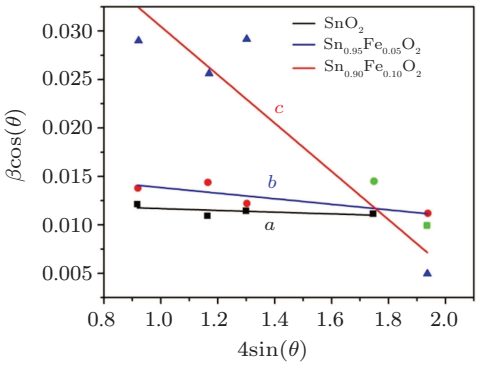


Fig. 2. UDM plots of (curve a) undoped SnO_2, (curve b) $Sn_{0.95}Fe_{0.05}O_2$, and (curve c) $Sn_{0.90}Fe_{0.10}O_2$ nanoparticles.

Table 2. Geometrical parameters of SnO_2 and Fe-doped SnO_2.

Samples	Scherrer's formula	UDM		USDM			UDEDM			
	D (nm)	D (nm)	Strain ε (10^{-3})	D (nm)	Strain ε (10^{-3})	Stress σ (MPa)	D (nm)	Energy density U (kJ·m^{-3})	Strain ε (10^{-3})	Stress σ (MPa)
SnO_2	11.926	11.516	−0.90	10.528	−1.98	−272.53	10.528	74272	32.87	4518.6
$Sn_{0.95}Fe_{0.05}O_2$	10.497	8.658	−2.87	8.658	−2.87	−394.9	8.658	567.39	2.873	394.95
$Sn_{0.90}Fe_{0.10}O_2$	4.9929	2.615	−24.9	2.615	−24.90	−3423	2.6148	42620	24.901	3423.0

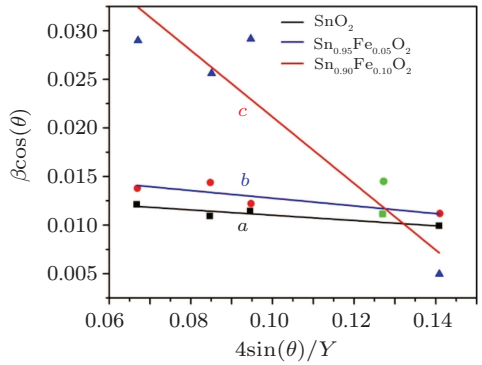


Fig. 3. USDM plot of (curve *a*) undoped SnO_2, (curve *b*) $Sn_{0.95}Fe_{0.05}O_2$, and (curve *c*) $Sn_{0.90}Fe_{0.10}O_2$ nanoparticles.

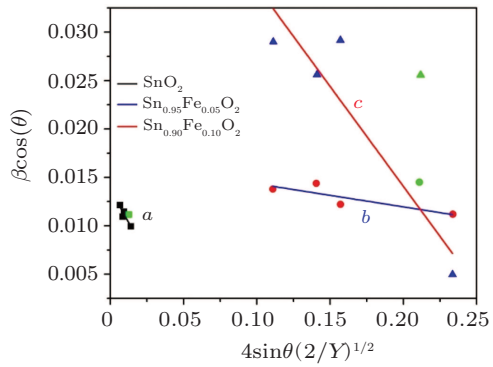


Fig. 4. UDEDM plot of (curve *a*) undoped SnO_2, (curve *b*) $Sn_{0.95}Fe_{0.05}O_2$, and (curve *c*) $Sn_{0.90}Fe_{0.10}O_2$ nanoparticles.

3.3. Optical analysis

3.3.1. UV–diffuse reflectance spectrum

The optical characterizations of the undoped and Fe-doped SnO_2 nanoparticles are performed by using UV-DRS spectroscopic measurements recorded in a range from 200 nm to 700 nm. The reflectance and absorbance spectra of the undoped and doped samples obtained are shown in Figs. 5 and 6 respectively. The absorption edge located around 300 nm is found to get red-shifted as doping concentration increases.[38]

A broad absorption peak with a width of 500 nm is also observed which is due to incorporation of Fe^{3+} into SnO_2 lattice and surface. It is observed from the XRD plot that the addition of Fe causes the crystallinity of sample to significantly decrease.[44] The precursor used has Fe in the oxidation state 3+ and the peak broadening clearly indicates the influence of Fe^{3+}. The Fe^{3+} ions occupy regular lattice sites causing the point defects and charge compensation effect which results in the distortion of crystal structure stoichiometry. The aggregation of Fe_2O_3 also reduces the growth of SnO_2 nanoparticles with the increase of dopant concentration. The optical band gap of the sample is estimated by considering the Kubelka–Munk function $F(R_\infty)$ for direct allowed transitions. Figure 7 shows the variation of $(F(R_\infty)h\nu)^2$ with photon energy $h\nu$, whose extrapolation of the linear portion gives the optical bandgaps 3.52 eV, 3.26 eV, and 2.28 eV respectively for undoped, 5-wt% doped, and 10-wt% Fe-doped SnO_2 nanoparticles.[45,46]

With the increase in dopant concentration a red shift is observed in the reflectance/ absorbance edge which confirms the incorporation of Fe^{3+} ions into the tin oxide lattice.[47] The conduction band or valence band of tin-oxide and Fe^{3+} ions can have charge transitions which might result in the electron concentration shift which can be corroborated with the red shift. The observed peak in the visible region centered around 550 nm corresponds to the characteristic peak of iron. As reported in Refs. [35,48] this can be attributed to the transitions between half-filled 'd' levels $(d \cdot d)$ of Fe^{3+} ions $(2T_{2g} \longrightarrow {}^2A_{2g}, {}^2T_{1g})$ or by the charge transfer between interacting iron atoms $(Fe^{3+} + Fe^{3+} \longrightarrow Fe^{4+} + Fe^{2+})$. Harve and Vandamme's model[49] is employed to calculate the refractive index through using the estimated band gap. The calculated values are tabulated in Table 3 and are in agreement with the reported values.[50,51]

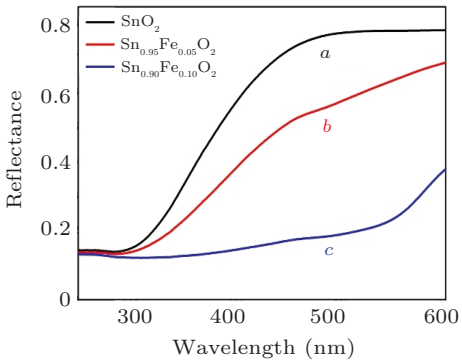


Fig. 5. UV-reflectance spectra of (curve *a*) undoped SnO_2, (curve *b*) $Sn_{0.95}Fe_{0.05}O_2$, and (curve *c*) $Sn_{0.90}Fe_{0.10}O_2$ nanoparticles.

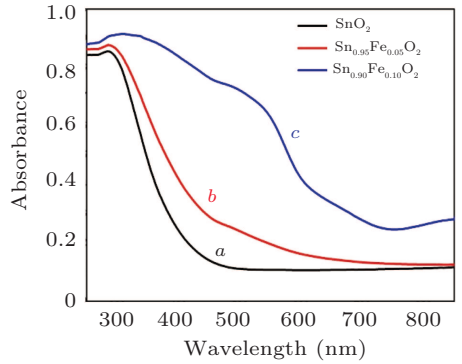


Fig. 6. UV-absorbance spectra of (curve *a*) undoped SnO_2, (curve *b*) $Sn_{0.95}Fe_{0.05}O_2$, and (curve *c*) $Sn_{0.90}Fe_{0.10}O_2$ nanoparticles.

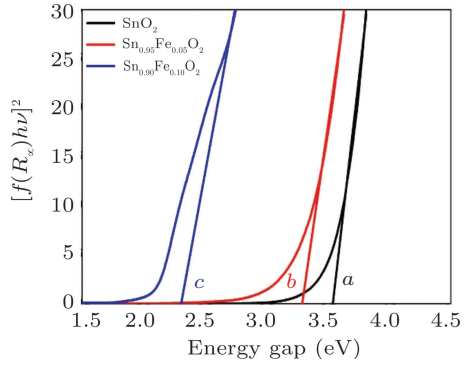


Fig. 7. UV-DRS plot of (curve *a*) undoped SnO_2, (curve *b*) $Sn_{0.95}Fe_{0.05}O_2$, and (curve *c*) $Sn_{0.90}Fe_{0.10}O_2$ nanoparticles.

Table 3. Refractive indexes of SnO_2 and Fe-doped SnO_2.

Sample	Herve and Vandamme	Moss
SnO_2	2.208	2.281
$Sn_{0.95}Fe_{0.05}O_2$	2.276	2.325
$Sn_{0.90}Fe_{0.10}O_2$	2.690	2.610

3.3.2. Photoluminescence spectra

The photoluminescence (PL) spectra are recorded at an excitation wavelength of 300 nm. The PL spectra of the synthesized nanoparticles shown in Fig. 8 contain emissions in the visible range from 400 nm to 500 nm with peaks centered at 2.9 eV (425 nm) and 2.6 eV (465 nm). The maximum emission centered at 2.6 eV corresponds to the energy lower than the band gap (3.6 eV) of bulk SnO_2. These peaks as well as the peaks centered on 2.9 eV can be ascribed to the defects or vacancies The intense emission in the visible region might be due to recombination of a large number of trapped states which result from solution-based synthesis process.[33]

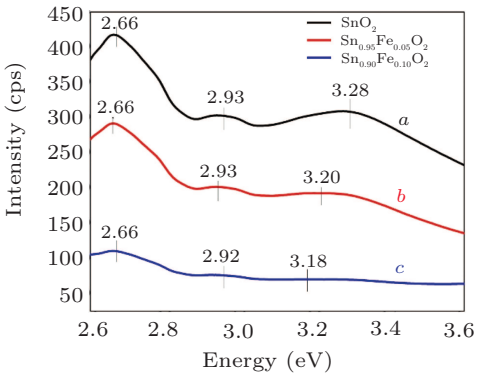


Fig. 8. The PL spectra of undoped SnO_2 (curve *a*), $Sn_{0.95}Fe_{0.05}O_2$ (curve *b*), and $Sn_{0.90}Fe_{0.10}O_2$ (curve *c*) nanoparticles.

The emission centred at 3.2-eV peak can stem from the band edge emission and the peak corresponding to 2.9 eV originates from luminescence center formed by tin interstitials or dangling bonds in the SnO_2 nanoparticles.[52] As the doping concentration of Fe^{3+} increases, non-radiative recombination will occur after the trapping of electrons and holes at the surface which can arise from the quenching of Pl intensity. Above the solubility limit, most of the Fe^{3+} gets precipitated into ferrous oxide phase and the excess Fe^{3+} phase resides at surface or grain boundary[53] as already explained in XRD analysis. The segregation of Fe3+ induces more compressive strain, thereby reducing the crystallinity of lattice. From the PL spectrum it is quite visible that the surface defects dominate over others because of the nanometer particle size which is also indicated from the strain analysis.

3.3.3. FT-Raman spectra

Analyses of the vibrational properties and effects of doping on them are carried out by using FT Raman spectra in a wavenumber range of 400 cm^{-1}–900 cm^{-1}. The unit cell of SnO_2 comprised of 2 tin atoms and 4 oxygen atoms in the center of brillouin zone, giving rise to 18 modes of vibration. The representation in the mechanical form is given by[54]

$$\Gamma = \Gamma_1^+(A_{1g}) + \Gamma_2^+(A_{2g}) + \Gamma_3^+(B_{1g}) + \Gamma_4^+(B_{2g}) + \Gamma_5^-(E_g) + 2\Gamma_1^-(A_{2u}) + 2\Gamma_4^-(B_{1u}) + 4\Gamma_5^+(E_u). \quad (6)$$

Among these, A_{1g}, B_{1g}, B_{2g}, and E_g are the four modes that arise from the vibration of oxygen atom around the tin atoms. The active modes A_{1g}, B_{1g}, B_{2g} have vibrations of oxygen atoms with planes perpendicular to the C axis and A_{2u} and E_u are the modes that involve dipole moments and hence they are Raman-inactive.

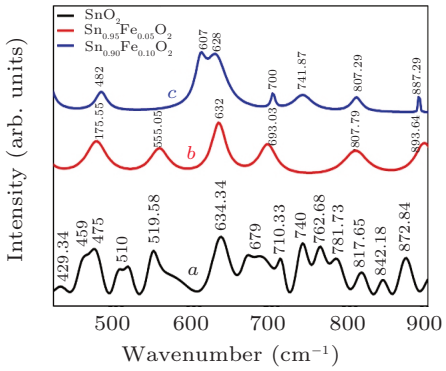


Fig. 9. Raman spectra of (curve *a*) undoped SnO_2, (curve *b*) $Sn_{0.95}Fe_{0.05}O_2$, and (curve *c*) $Sn_{0.90}Fe_{0.10}O_2$ nanoparticles.

As reported in Ref. [55], the bulk SnO_2 shows peaks around 466, 635, 757 cm^{-1} which can be ascribed to the E_g, A_{1g}, and B_{2g} modes. It is observed that each of all the three bands with a shift is observed in the synthesized samples also, confirming rutile nature of SnO_2. Apart from the fundamental vibrations, a few additional bands at 510, 549, 710, 740, 781, 817, and 842 cm^{-1} are also observed. These additional bands appear because the surface properties of the crystal depend on the oxygen vacancy, other disorder along with grain size and its distributions.[56] The bands in 549 cm^{-1} is red-shifted and 634 cm^{-1} is blue-shifted, hence showing the effect of grain boundaries on the functional spectra and vibrational spectra of tin oxide. The band 679 cm^{-1} and 700 cm^{-1} observed in SnO_2 and Fe(5 wt%, 10 wt%)-doped SnO_2 correspond to IR-active A_{2u} modes.[57] The continuous broadening in Raman peaks with the decrease in crystalline size can be ascribed to phonon confinement effect. As confirmed from the x-ray diffraction analysis a reduction in crystallinity occurs with the grain boundary formation which causes the phonon dispersions to occur near the zone center. Thus, the activation of inactive mode and shift of band can take place as a result of the Fe incorporation. The incorporation of Fe into the grain boundary results in trapped states and electron hole recombination which causes the Raman modes to decrease with the increase in Fe-dopant concentration. This is also in correlation with quenching observed in PL.[58] The spectral band transitions of 817 cm^{-1} and 895 cm^{-1} can be ascribed to the stretching vibration of double coordinated SnO_2.[59]

3.3.4. Field emission scanning electron microscopy

The morphological and compositional analyses of SnO_2, $Sn_{0.95}Fe_{0.05}O_2$, and $Sn_{0.90}Fe_{0.10}O_2$ nanoparticles obtained by using FESEM and EDAX spectra, and the results are shown in Fig 10.

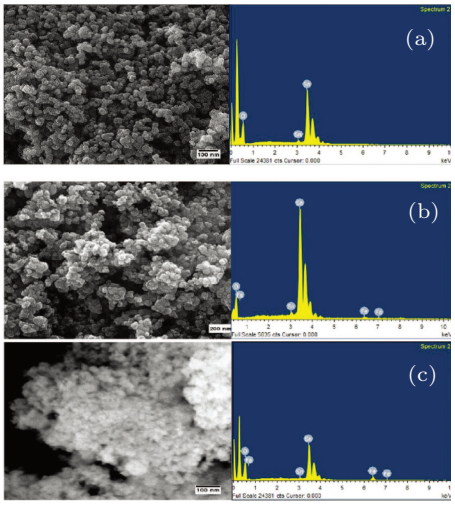


Fig. 10. FESEM micrograph and EDAX spectra of (a) undoped SnO_2 nanoparticles, (b) $Sn_{0.95}Fe_{0.05}O_2$, and (c) $Sn_{0.90}Fe_{0.10}O_2$ nanoparticles.

The micrograph clearly displays the influence of dopant concentration on the surface morphology of the nano powder. The structure shows homogeneously well dispersed spherical nanoparticles aggregated into the irregularly shaped tin oxide nanoparticles. Grains of each sample consist of large aggregates which transform into the fine aggregates with the increase in Fe dopant concentration. The average grain size obtained by using the Image J analysis of the undoped SnO_2 is around 10 nm accounting for 5 wt% and around 13 nm occupying 10 wt%, indicating the aggregation of particles and grain boundaries. The formation of irregular shape can be ascribed to the grain rotation.[60]

The grain rotation leads the neighboring grains to coalesce by eliminating the common grain boundary between them. It is one of the mechanisms for growth. The driving force for rotation is the net torque which arises from the variation in rate of diffusion as observed in XRD. The grains embedded in a polycrystal are subjected to a torque which can be reduced by the grain rotation. This rotation creates a void in other region because of the overlap of grains. This gives rise to the regions of compression and tension along the grain perimeter,[61] as explained in Williamson–Hall method which set up diffusion fluxes to accommodate the rotation. The increase in density of particles confirms the segregation of particles from boundaries. It is also reported that surfactant plays a major role in this coagulation and segregation after the nucleation.

The compositional analysis of the sample is conducted by energy dispersive x-ray spectroscopy (EDAX) (Fig. 10). It is clear from the EDAX spectra that Sn and O are the only main elemental species in as-prepared SnO_2, though additional Fe peaks are observed in the spectra of doped samples. The elemental compositions obtained by the sol-gel method show the values approximately equal to that estimated from synthesis conditions.

4. Conductivity studies

4.1. Impedance analysis

The variation in the dielectric nature of the SnO_2 with Fe-doping concentration is analyzed by using LCR meter in a frequency range of 50 Hz–5 MHz. The electrical impedance (Z), dielectric loss factor ($\tan\delta$), AC conductivity of undoped and doped SnO_2 samples are analyzed. The frequency dependence of dielectric constant and the influence of doping on it are studied in detail by taking the real and imaginary components of dielectric constant[62]

$$\varepsilon^* = \varepsilon' - j\varepsilon''. \tag{7}$$

The variations of real part for dielectric constant (ε') with frequency for SnO_2 and Fe-doped SnO_2 are shown in Fig. 11. The dielectric constant decreases with the increase in frequency and at high frequencies it becomes constant. The frequency dependence on dielectric constant is prominent in the low frequency regions. The dielectric constant is found to decrease as the frequency increases and then reaches a constant value at higher frequencies. The FESEM images of SnO_2 nanoparticles reveal their inhomogeneous structures. The dipoles oscillating under such fields will follow the field, and dielectric constant value equals the dielectric constant in a quasi static field. As the frequency increases, the dipoles begin to lag the field and then stop following the field when the frequency is above the characteristic frequency. The oscillation of charge carriers cannot happen simultaneously with switching at high frequency, and the rapid polarization reaches a constant value at high frequency.[63] The dielectric constant value of Fe-doped SnO_2 nanoparticles drastically decreases which can be attributed to the grain boundary effect. The application of external field results in coalitions of grain boundaries and a very little polarization under these conditions at high frequencies can cause the dielectric constant values to lower. The same trend is observed for imaginary parts also (Fig. 12).[11] The conduction losses by the charge carriers, ionic hopping or ionic polarization can lead the value of ε'' to increase at low temperature. The decrease of imaginary part of dielectric constant is due to the space charge polarization occurring at higher frequencies.[64]

The phase difference, with the applied field leading to the drop in the dielectric value, is known as loss factor tangent[65]

$$\tan\delta = \varepsilon''/\varepsilon'. \tag{8}$$

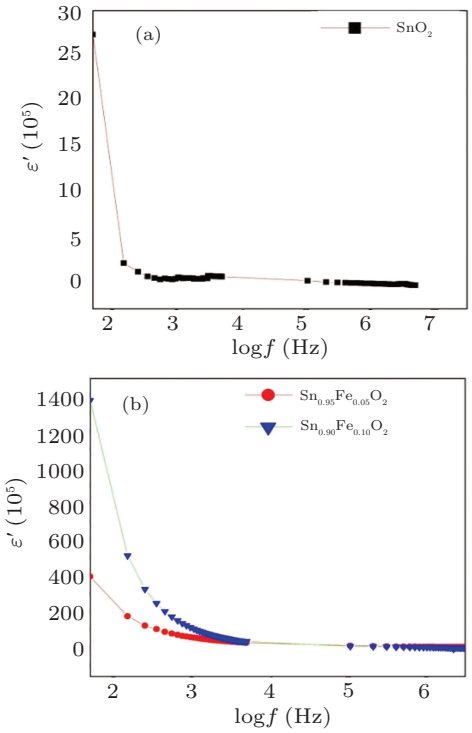


Fig. 11. Variations of dielectric constant (ε') with frequency for (a) undoped SnO_2, (b) $Sn_{0.95}Fe_{0.05}O_2$, and $Sn_{0.90}Fe_{0.10}O_2$ nanoparticles.

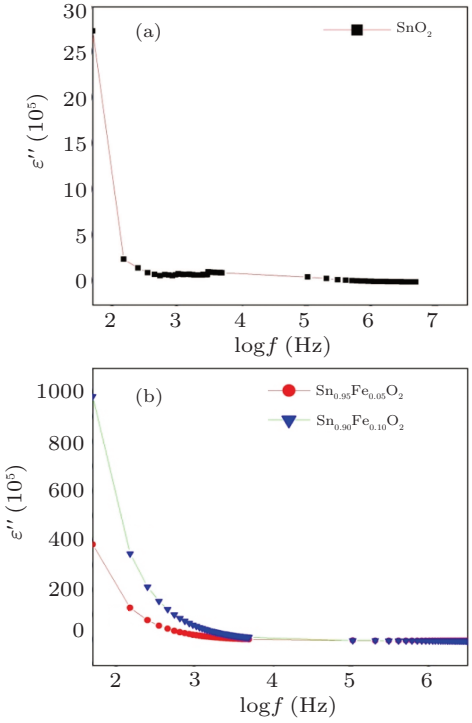


Fig. 12. Frequency dependence of dielectric constant (ε'') of (a) undoped SnO_2, (b) $Sn_{0.95}Fe_{0.05}O_2$, and $Sn_{0.90}Fe_{0.10}O_2$ nanoparticles.

The variations of loss tangent with log frequency in Fig. 13 show that the loss factor decreases invariably for all samples from in a frequency range from 50 Hz to 5 MHz. The Fe doping results in the formation of grain boundaries which are electrically resistive in nature, Based on Koop's theory, the dielectric value should be high at low frequencies, and dielectric relaxation occurs beyond characteristic frequency. It is also observed that dielectric loss decreases with Fe doping concentration increasing, hence Fe doping concentration above the solubility limit in SnO_2 can get a material suitable for high frequency applications.[64]

The variations of alternating current (AC) conductivity with log frequency for SnO_2 and 5-wt% and 10-wt% Fe-doped SnO_2 are shown in Fig. 14. The AC conductivity of SnO_2 and Fe-doped SnO_2 are analyzed using the relation[11]

$$\sigma_{ac} = 2\pi\varepsilon_0\varepsilon' f \tan\delta. \tag{9}$$

The charge carriers in the trapped states overcome the potential barrier with the increase of frequency, thus contributing to conduction. The rapid increase in conductivity occurs when charge carriers gain enough energy to overcome the potential barrier.[66]

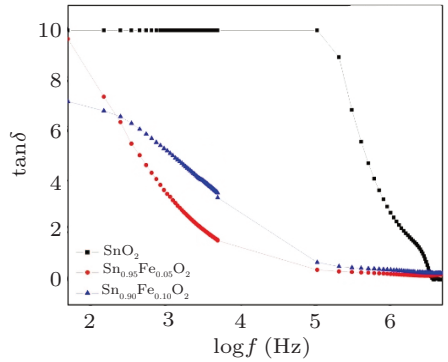


Fig. 13. Variations of dielectric loss factor ($\tan\delta$) with log frequency for undoped SnO_2, $Sn_{0.95}Fe_{0.05}O_2$, and $Sn_{0.90}Fe_{0.10}O_2$ nanoparticles.

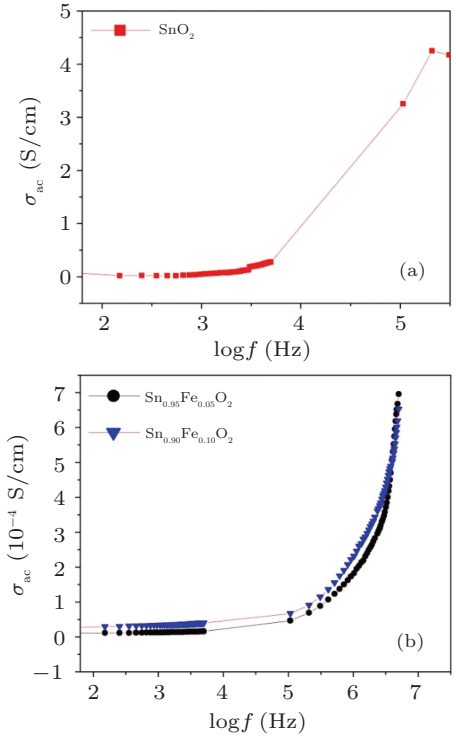


Fig. 14. Frequency-dependent AC conductivity of (a) undoped SnO_2, (b) $Sn_{0.95}Fe_{0.05}O_2$, and $Sn_{0.90}Fe_{0.10}O_2$ nanoparticles.

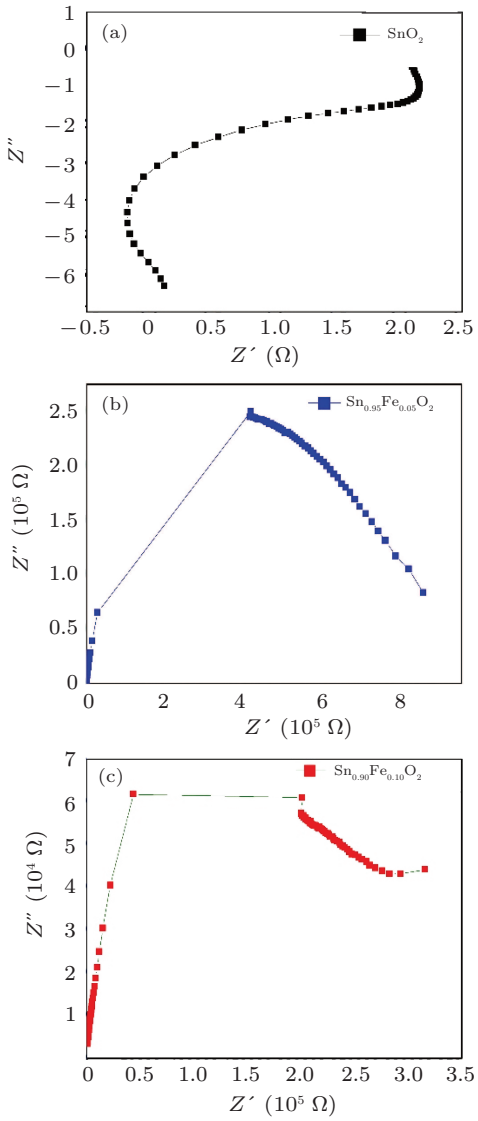


Fig. 15. Nyquist plot of (a) undoped SnO_2, (b) $Sn_{0.95}Fe_{0.05}O_2$, and (c) $Sn_{0.90}Fe_{0.10}O_2$ nanoparticles.

To obtain the detailed information about the contribution of grain boundaries and grains, the capacitance and resistance components in the impedance are plotted in the complex plane. Figure 15 shows the Nyquist plots which indicate slight semicircle behaviors for all samples. The diameter of semicircular pattern increases with doping concentration increasing, indicating that the impedance increases with doping concentration increasing.[67]

4.2. DC conductivity

Using a two-probe model, as-prepared SnO_2 and iron-doped SnO_2 samples are analyzed between room temperature and 120 °C to obtain the parameters like conductivity (σ_{dc}), resistivity (ρ), and activation energy (E_a). Figure 16 shows I–V characteristic curves of SnO_2 and Fe(5 wt% and 10 wt%)-doped SnO_2. With applied voltage increasing, the current value linearly increases for each of all samples. With the increase in dopant concentration, the current value decreases, but the samples show significant temperature dependence. For as-prepared SnO_2 sample, the current values show constant linear behavior with variation in temperature. As the dopant concentration increases, the current values change considerably with the temperature, showing a highest current value at 120 °C.

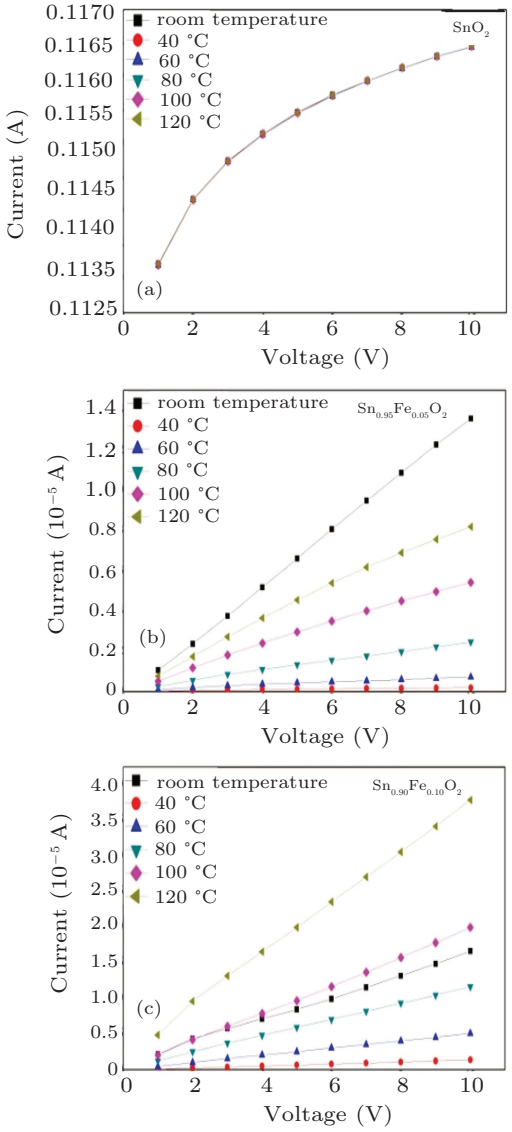


Fig. 16. The I–V characteristics of (a) undoped SnO_2, (b) $Sn_{0.95}Fe_{0.05}O_2$, and (c) $Sn_{0.90}Fe_{0.10}O_2$ nanoparticles.

The DC conductivity is calculated from the following equation[68]

$$\sigma_{dc} = \frac{t}{RA}\ \mathrm{S/cm}, \tag{10}$$

where t is pellet thickness, R is resistance, and A is pellet area.

From Table 4, it is observed that the calculated σ_{dc} values of the samples decrease gradually with the increase in Fe-doping concentration in a range from 10^{-4} S/cm to 10^{-7} S/cm.

Initially the carrier concentration decreases with Fe^{3+}-doping concentration increasing and then remains almost the same (with only small variations). The carrier concentration decreases because Fe^{3+} creates a positively charged hole and segregates electrically inactive Fe atoms into the grain boundary.[69]

Table 4. Values of resistivity and conductivity of samples.

Sample	Resistivity ρ (Ω/cm)	Conductivity σ_{dc} (S/cm)
SnO_2	3.372×10^3	2.97×10^{-4}
$Sn_{0.95}Fe_{0.05}O_2$	1.079×10^8	4.60×10^{-8}
$Sn_{0.90}Fe_{0.10}O_2$	2.165×10^7	1.45×10^{-7}

It is observed that conductivity of individual sample increases with temperature increasing, which shows the semiconducting nature of the sample. The increase in resistivity with Fe-doping concentration increasing is due to segregation of dopants into the boundary. Figure 17 shows the Arrhenius plot, *i.e.*, $(1/T)$ (K^{-1}) *versus* $\ln\sigma_{dc}$ (S/cm). As the dopant concentration increases beyond the solid solubility limit it will get clustered in the material boundaries, thus reducing the electron concentration, and the conductivity will fall at a certain doping concentration.[62] The semiconducting property is found to be enhanced with Fe doping at 10 wt% as the grain boundary blocking effect which reduces the conductivity is negated at high temperatures and higher doping concentrations.[62]

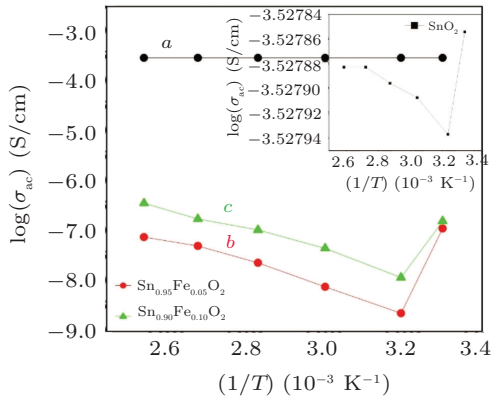


Fig. 17. The Arrhenius plot of (cure *a*) undoped SnO_2, (cure *b*) $Sn_{0.95}Fe_{0.05}O_2$, and (cure *c*) $Sn_{0.90}Fe_{0.10}O_2$ nanoparticles.

5. Conclusions

The SnO_2 and Fe-doped SnO_2 nanoparticles are synthesized by using the simple sol–gel method.

The decrease in crystallinity obtained from the XRD confirms the formation of grain boundaries. The decrease in the band gap is measured by using UV DRS analysis, the photoluminescence, and Raman spectra also confirm the grain boundary influence on the properties of SnO_2 nanoparticles. The field emission scanning electron microscope images reveal the Fe-doped inhomogeneous grain boundary formation. The conductivity studies performed on this material show that the Fe doping increases the impedance of the material and the dielectric loss tangent decreases with doping concentration increasing at high frequencies. The semiconducting natures of the samples are found to be enhanced as grain boundary blocking effect decreases at high temperature and higher doping concentration. Thus, the doping of Fe above the solubility limit forms the grain boundary, which can be used as a material for high-frequency detection application.

Acknowledgment

The authors thank the support rendered by Dr. A Karthega, Amrita Vishwa Vidyapeetham for the facilitation of experimental part, and also thank SRMV Advanced Research Instrumentation Center, Coimbatore for their helps with UV, PL, and dielectric measurements, and SAIF, IIT Madras for FT-Raman measurement. Authors also thank Karunya University for XRD measurements and SITRA and CIT, Coimbatore for FESEM and EDAX measurements.

References

[1] Chavali M S and Nikolova M P 2019 *SN Appl. Sci.* **1** 607
[2] Bajpai N, Khan S A, Kher R S, Bramhe N, Dhoble S J and Tiwari A 2014 *J. Lumin.* **145** 940
[3] Jiang Q, Zhang X and You J 2018 *Nano-Micro Small* **14** 1
[4] Carre? no N L V, Nunes M R, Garcia I T S, Orlandi M O, Fajardo H V and Longo E 2009 *J. Nanoparticle Res.* **11** 955
[5] Batzill M and Diebold U 2005 *Prog. Surf. Sci.* **79** 47
[6] Doke S, Ganguly P and Mahamuni S 2020 *D Liq. Cryst.* **00** 1
[7] Li H, Su Q, Kang J, Huang M, Feng M, Feng H, Huang P and Du G 2018 *Mater. Lett.* **217** 276
[8] Elango G and Roopan S M 2016 *E J. Photochem. Photobiol. B Biol.* **155** 34
[9] Viet P Van, Thi C M and Hieu L Van 2016 *J. Nanomater.* **2016**
[10] Li Z and Yi J 2017 *Sensors Actuators B Chem.* **243** 96
[11] Hermawan A, Asakura Y, Inada M and Yin S 2019 *Ceram. Int.* **45** 15435
[12] Xie H, Yin X, Chen P, Liu J, Yang C, Que W and Wang G 2019 *Mater. Lett.* **234** 311
[13] Karthik K, Revathi V and Tatarchuk T 2018 *Mol. Cryst. Liq. Cryst.* **671** 17
[14] Arularasu M V, Anbarasu M, Poovaragan S, Sundaram R, Kanimozhi K, Magdalane C M, Kaviyarasu K, Thema F T, Letsholathebe D, Mola G T and Maaza M 2017 *J. Nanosci. Nanotechnol.* **18** 3511
[15] Shanmugam N, Sathya T, Viruthagiri G, Kalyanasundaram C, Gobi R and Ragupathy S 2016 *Appl. Surf. Sci.* **360** 283
[16] Patil G E, Kajale D D, Gaikwad V B and Jain G H 2012 *Int. Nano Lett.* **2** 2
[17] Zhang J and Gao L 2004 *S J. Solid State Chem.* **177** 1425
[18] Marzec A, Radecka M, Maziarz W, Kusior A and Pedzich Z 2016 *S J. Eur. Ceram. Soc.* **36** 2981
[19] Voon C H, Foo K L, Lim B Y, Gopinath S C B and Al-Douri Y 2020 *Synthesis and Preparation of Metal–Oxide Powders, Metal Oxides* ed Al-Douri (Elsevier) pp. 31–65
[20] Al-Samarai R A, Mahmood A S and Al-Douri Y 2020 5 *Metal Oxides* ed Al-Douri (Elsevier) pp. 83–99
[21] Wang E, Chen P, Yin X, Wu Y and Que W 2019 *Sol. RRL* **3** 1
[22] Alexandrescu R, Morjan I, Dumitrache F, Birjega R, Fleaca C, Luculescu C R, Popovici E, Soare I, Sandu I, Dutu E and Prodana G 2010 *J. Optoelectron. Adv. Mater.* **12** 599
[23] Tian Z M, Yuan S L, He J H, Li P, Zhang S Q, Wang C H, Wang Y Q, Yin S Y and Liu L 2008 *J. Alloys Compd.* **466** 26
[24] Toloman D, Popa A, Stan M, Socaci C, Biris A R, Katona G, Tudorache F, Petrila I and Iacomi F 2017 *Appl. Surf. Sci.* **402** 410
[25] Dorneanu P P, Airinei A, Grigoras M, Fifere N, Sacarescu L, Lupu N and Stoleriu L 2016 *J. Alloys Compd.* **668** 65
[26] Mani R, Vivekanandan K and Vallalperuman K 2017 *J. Mater. Sci. Mater. Electron.* **28** 4396
[27] Kaur N, Abhinav, Singh G P, Singh V, Kumar S and Kumar D 2016 *AIP Conf. Proc.* **1728** 1
[28] Barkley T K, Vastano J E, Applegate J R and Bakrania S D 2012 *Adv. Mater. Sci. Eng.* **2012**
[29] Tran R, Xu Z, Zhou N, Radhakrishnan B, Luo J and Ong S P 2016 *Acta Mater.* **117** 91

[30] Ben Haj Othmen W, Sdiri N, Elhouichet H and Férid M 2016 *Mater. Sci. Semicond. Process.* **52** 46

[31] Garnet N S, Ghodsi V, Hutfluss L N, Yin P, Hegde M and Radovanovic P V 2017 *J. Phys. Chem. C* **121** 1918

[32] Cullity B D 1956 *Elements of X-ray Diffraction* (Addison-Wesley Publishing)

[33] Kaur J, Shah J, Kotnala R K and Verma K C 2012 *R Ceram. Int.* **38** 5563

[34] Sabri N S, Deni M S M, Zakaria A and Talari M K 2012 *Phys. Procedia* **25** 233

[35] Asiltürk M and Sayılkan F 2009 *J. Photochem. Photobio. A* **203** 64

[36] Liu C M, Fang L M, Zu X T and Zhou W L 2007 *Chin. Phys.* **16** 95

[37] Chang C H, Gong M, Dey S, Liu F and Castro R H R 2015 *J. Phys. Chem. C* **119** 6389

[38] Pereira M S, Ribeiro T S, Lima F A S, Santos L P M, Silva C B, Freire P T C and Vasconcelos I F 2018 *J. Nanoparticle Res.* **20** 2029

[39] Rani S, Roy S C, Karar N and Bhatnagar M C 2007 *Solid State Commun.* **141** 214

[40] Rohith N M, Kathirvel P, Saravanakumar S and Mohan L 2018 *Optik (Stuttg.)* **172** 940

[41] Bindu P and Thomas S 2014 *J. Theor. Appl. Phys.* **8** 123

[42] A Narmada, P Kathirvel, Mohan L, S Saravanakumar, R Marnadu and J Chandrasekhar 2020 *Optik (Stuttg.)* **202** 163701

[43] Muhammed Shafi P and Chandra Bose A 2015 *AIP Adv.* **5** 057137

[44] Fang L M, Zu X T, Li Z J, Zhu S, Liu C M, Zhou W L and Wang L M 2008 *J. Alloys Compd.* **454** 261

[45] Winyayong A and Wongsaprom K 2019 N *Journal of Physics: Conference Series* Vol. 1380

[46] Mohan L, Sisupalan N, Ponnusamy K and Sadagopalan S 2020 *J. Inorg. Organomet. Polym. Mater.* **30** 2626

[47] Babu B, Neelakanta Reddy I, Yoo K, Kim D and Shim J 2018 *Mater. Lett.* **221** 211

[48] Adán C, Bahamonde A, Fernández-García M and Martínez-Arias A 2007 *Appl. Catal. B Environ.* **72** 11

[49] Kumar V and Singh J K 2010 *Indian J. Pure Appl. Phys.* **48** 571

[50] Haouanoh D, TalaIghil R Z, Toubane M, Bensouici F and Mokeddem K 2019 *Mater. Res. Express* **6** 086422

[51] Zadsar M, Fallah H R, Haji Mahmoodzadeh M, Hassanzadeh A and Ghasemi Varnamkhasti M 2012 *Mater. Sci. Semicond. Process.* **15** 432

[52] Gu F, Wang S F, Song C F, Lü M K, Qi Y X, Zhou G J, Xu D and Yuan D R 2003 *Chem. Phys. Lett.* **372** 451

[53] Gu F, Wang S F and Lu M K 2004 *Photoluminescence Properties of SnO_2 Nanoparticles Synthesized by Sol–Gel Method* 8119–23

[54] Romano-rodrı A 2001 T *J. Appl. Phys.* **90** 1550

[55] Das S, Kar S and Chaudhuri S 2006 *J. Appl. Phys.* **99** 058201

[56] Ben W, Othmen H, Sieber B, Elhouichet H, Addad A, Gelloz B, Moreau M, Szunerits S and Boukherroub R 2018 *Mater. Sci. Semicond. Process.* **77** 31

[57] Abello L, Bochu B, Gaskov A, Koudryavtseva S, Lucazeau G and Roumyantseva M 1998 *J. Solid State Chem.* **135** 78

[58] Periyasamy M and Kar A 2020 *J. Mater. Chem. C* **8** 4604

[59] Shajira P S, Prabhu V G and Bushiri M J 2015 *J. Phys. Chem. Solids* **87** 244

[60] Moldovan D, Wolf D, Phillpot S R and Haslam A J 2003 *Trends in Nanoscale Mechanics* pp. 35–59

[61] Moldovan D, Wolf D and Phillpot S R 2001 *Acta Mater.* **49** 3521

[62] Barik Subrat, Choudhary R N and Singh A K 2011 *Adv. Mater. Lett.* **2** 419

[63] Chenari H M, Hassanzadeh A, Golzan M M, Sedghi H and Talebian M 2011 *Curr. Appl. Phys.* **11** 409

[64] Khan R and Fashu S 2017 *J. Mater. Sci. Mater. Electron.* **28** 4333

[65] Azam A, Ahmed A S, Ansari M S, M M S and Naqvi A H 2010 *J. Alloys Compd.* **506** 237

[66] Ashokkumar M and Muthukumaran S 2015 *J. Lumin.* **162** 97

[67] Wang C J, Wang Y and Gao C X 2019 *Acta Phys. Sin.* **68** 206401 (in Chinese)

[68] Marnadu R, Chandrasekaran J, Maruthamuthu S, Balasubramani V, Vivek P and Suresh R 2019 *Appl. Surf. Sci.* **480** 308

[69] Soitah T N, Yang C and Sun L 2011 *Mater. Sci. Semicond. Process.* **13** 125